Polymer Journal (2013) 45, 79–86

www.nature.com/pj

ORIGINAL ARTICLE

Simultaneous small- and wide-angle X-ray scattering studies on the crystallization dynamics of poly(4-methylpentene-1) from melt

Kazuki Mita[1], Hiroshi Okumura[1], Kazuki Kimura[1], Takeharu Isaki[1], Mikihito Takenaka[2,3] and Toshiji Kanaya[4]

The crystallization process of poly(4-methylpentene-1) (P4MP1) under an isothermal condition at 227 °C was investigated by means of simultaneous small- and wide-angle synchrotron radiation X-ray scattering. The changes in the lamella structure and in the crystal lattice were elucidated for the first time; the thickness of the lamellae along the chain axis was constant during crystallization, whereas the lattice constant along the *a*-axis changed to the most stable value. We also found that crystallization consists of two processes and that there is an inhomogeneous structure even in the melt and in the induction period before crystallization. These features of P4MP1 were compared with those of other polymers, and we discussed the changes in the crystal lattices and in the lamella thickness during the crystallization process.
Polymer Journal (2013) **45,** 79–86; doi:10.1038/pj.2012.204; published online 21 November 2012

Keywords: poly(4-methylpentene-1); scattering; SPring-8

INTRODUCTION

Poly(4-methylpentene-1) (P4MP1) is a crystalline polyolefin that is an important industrial material because of its advantageous properties, such as heat resistance (high melting temperature), light weight (low density), release properties (low surface tension) and excellent transparency. These properties, especially the high melting temperature and the low density, are also intriguing from a scientific point of view. The high melting temperature corresponds to the significantly lower entropy of fusion of P4MP1 compared with other polyolefin,[1,2] and the lower entropy of fusion relates to the existence of an inhomogeneous structure in the melt.[3,4] The low density is a result of the extraordinarily low density of the crystals. The extraordinarily low density of the crystals is due to '*interlocking*' of the large side groups inside the crystals along the direction perpendicular to the chain axis (*c*-axis).[5]

To take advantage of the properties of P4MP1, we have to control its morphology. There are several reports on the crystal lattice structure of P4MP1.[5–21] According to these reports, P4MP1 has four types of polymorphisms, and the most stable crystalline form, which is often called Form I, can be obtained via crystallization from the melt. Form I consists of helical polymer chains with a 7_2 helix, and the helices form a tetragonal lattice with four chains per unit cell. In the tetragonal lattice, *interlocking* is present. The lattice parameters are $a = b = 18.70$ Å, $c = 13.68$ Å and $\alpha = \beta = \gamma = 90°$.[5]

P4MP1 processing, such as extrusion and injection molding, consists of crystallization from the melt, so the resulting crystal lattice is always the tetragonal lattice that exhibits *interlocking*. Therefore, to control the properties of P4MP1, we have to understand and control the higher order structures in its hierarchy. Specifically, elucidating the lamella structures is essential for controlling the hierarchical structures. However, there are few reports about the lamella structures using small-angle X-ray scattering (SAXS).[22,23] SAXS is one of the most effective methods for studying the lamella structures of crystalline polymers. One of the reasons that there are few SAXS studies on P4MP1 is that the P4MP1 crystallized from melt state has an unusual closeness between the densities of the crystal (ρ_c) and that of the amorphous (ρ_a), especially at room temperature, and this closeness makes the SAXS intensity too weak to allow detection of the structures. Tanigami *et al.*[22] used static SAXS measurements to determine that the density difference ($\Delta\rho$) between ρ_c and ρ_a increases with temperature, which is consistent with the result obtained by Grifith and Rånby,[24] and that the SAXS intensity increases as the sample temperature increases. Silvestre *et al.*[23] utilized this temperature dependence of $\Delta\rho$ and, by using SAXS at 100 °C, statically observed that the lamella structure of the samples crystallized under several conditions. Another method for detecting the lamella structures of P4MP1 is electron microscopy,[25,26] but this method requires the cutting, staining or replicating of the sample, so

[1]Material Science Laboratory, Mitsui Chemicals Inc., Sodegaura, Chiba, Japan; [2]Department of Polymer Chemistry, Graduate School of Engineering, Kyoto University, Katsura, Nishikyo-ku, Kyoto, Japan; [3]Structural Materials Science Laboratory, SPring-8 Center, RIKEN Harima Institute Research, 1-1-1, Kouto, Sayo-cho, Sayo-gun, Hyogo and [4]Institute for Chemical Research, Kyoto University, Uji, Kyoto, Japan
Correspondence: Dr K Mita, Material Science Laboratory, Mitsui Chemicals Inc., 580-32 Nagaura, Sodegaura, Chiba 299-0265, Japan.
E-mail: Kazuki.Mita@mitsui-chem.co.jp
Received 29 June 2012; revised 28 September 2012; accepted 1 October 2012; published online 21 November 2012

observations are limited to static conditions. These reports provide important static information, but the lamella structures change depending on the method of crystallization. Therefore, it is necessary to dynamically explore and precisely determine the morphological changes in the lamella structure during the crystallization process. However, there are no reports on the dynamic changes that occur during crystallization. Moreover, the effects of the existence of an inhomogeneous structure in the melt and of the *interlocking* of the side groups on the dynamic changes have not been clarified. A few reports using dilatometry[24] and differential scanning calorimetry[27,28] mention the time evolution of the crystallization of P4MP1, but these methods cannot detect structures such as lamellae directly.

In this study, the crystallization process of P4MP1 under isothermal conditions was dynamically investigated by means of simultaneous small- and wide-angle synchrotron radiation X-ray scattering, and we report for the first time the crystal structure formation of P4MP1 over a wide spatial scale from 0.1 nm to several 100 nm, which involves the development of the lamella structure and the crystal lattice formation in the lamellae. We also discuss how the inhomogeneous structure in the melt and the *interlocking* of the side groups affect the crystallization of P4MP1.

EXPERIMENTAL PROCEDURE

The P4MP1 used in this study is a product of Mitsui Chemicals, Inc., Chiba, Japan (TPX) that has a weight-averaged molecular weight of $M_w = 2.7 \times 10^5$ and a polydispersity of $M_w/M_n = 3.2$, which were determined from gel permeation chromatography to be polystyrene-equivalent values. The melting temperature (T_m) of the P4MP1 is 240 °C, which was determined by differential scanning calorimetry with a heating rate of 10 °C min^{-1} and is close to the usually reported value.[29,30] The equilibrium melting temperature calculated using Hoffman–Weeks plots[31] was reported as 261 °C.[32] In order to obtain a film specimen 0.5 mm thick for the SAXS and wide-angle X-ray scattering (WAXS) measurements, the P4MP1 was melt-pressed at 260 °C and quenched by cold-pressing at 25 °C.

SAXS and WAXS measurements were simultaneously carried out using the beamline BL03XU at SPring-8, Hyogo, Japan.[33] The wavelength of the incident X-rays was 0.1 nm. A charge-coupled device camera with an image-intensifier and a flat panel detector were used as detectors in the SAXS and WAXS measurements, respectively. The sample-to-detector distances of the SAXS and WAXS measurements were 1735 and 83 mm, respectively. We subtracted the scattering intensity of an empty cell from that of the specimen by taking into account the transmittance of X-rays through the specimen to obtain the scattering intensity from the sample. The observed two-dimensional (2D) SAXS and WAXS patterns were isotropic and the one-dimensional (1D) intensities were evaluated as a function of q after a circular average of the 2D patterns was performed. Here, q is the magnitude of the scattering vector, $q = (4\pi/\lambda) \sin(\theta/2)$, where λ and θ are the wavelength of the incident X-rays and the scattering angle, respectively.

Time-resolved SAXS and WAXS measurements were performed on P4MP1 during the isothermal crystallization processes at $T_f = 227$ after a T-drop from the melt at $T_i = 264$ °C. SAXS and WAXS measurements were also collected for the melt state before the T-drop. The quenching process was performed as follows: first, the specimen was placed in a sample cell[34] with 12.5-μm-thick Kapton windows and then was put in a heater block at T_i (heater block I). After holding for 5 min at T_i to erase the thermal history of the sample, the cell was transferred into another heater block regulated at T_f (heater block II). When the transfer of the cell was completed, the time (t) was set to zero. The time-resolved simultaneous SAXS and WAXS measurements were started at $t = 47$ s. The temperature in the specimen reached the measuring temperature ($= T_f$) within ~90 s after the T-drop. Time-resolved measurements were collected every 5 s after the T-drop, and the exposure times for the SAXS and WAXS measurements were 200 and 500 ms, respectively, throughout this study.

RESULTS

First, we examined the formation of the crystal lattice detected by the time-resolved WAXS measurements. Figure 1 shows examples of the WAXS profiles obtained during the isothermal crystallization at 227 °C. The scattering profiles obtained for the melt state before the T-drop and 47 s after the T-drop ($t = 47$ s) exhibit amorphous halos composed of two broad peaks around $q = 6$ and 12 nm^{-1} (low-q and high-q peaks, respectively). To determine the origin of each peak, we evaluated the change in the correlation length (l) of the amorphous halo Δl before and after the T-drop, which is defined by Equation 1 for both the low-q and high-q peaks.

$$\Delta l = \frac{2\pi}{q_{m,i}} - \frac{2\pi}{q_{m,f}} \quad (1)$$

where $q_{m,i}$ and $q_{m,f}$ are the q-values at the maximum intensity of the corresponding peaks obtained before and 47 s after the T-drop ($t = 47$ s), respectively. The Δl values were 0.028 and 0.008 nm for the low- and high-q peaks, respectively. The temperature dependence of l is much larger for the low-q peak than for the high-q peak, suggesting that the low- and high-q peaks arise primarily from inter- and intramolecular correlations, respectively.

The scattering profile obtained at $t = 92$ s shows very weak but sharp peaks, which correspond to the diffraction from a crystal lattice with a tetragonal unit cell,[5] although the profile still shows that the amorphous halos have nearly the same intensity as at $t = 47$ s. After $t = 92$ s, the intensities of the sharp diffraction peaks increased with increasing t, whereas the intensities of the amorphous halos decreased with increasing t, indicating that the crystal lattice retained the tetragonal unit cell and that the volume occupied by the lattice increases with increasing t. In the inset of Figure 1, we magnified the diffraction peak from the (200) plane in order to see the small changes that occur. It is clear that the peak position moves with time, indicating a change in the size of the tetragonal unit cell. This issue

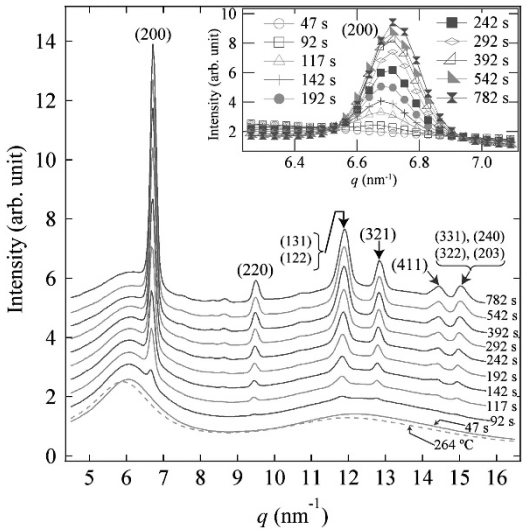

Figure 1 Time evolution of the wide-angle X-ray scattering (WAXS) profiles during isothermal crystallization at $T_f = 227$ °C. The scattering profile for the melt at $T_i = 264$ °C (dashed line) is also included. Scattering profiles except those obtained at T_i and $t = 47$ s were shifted vertically for clarity. In the inset, the diffraction peak from the (200) lattice plane is enlarged. Scattering profiles were not shifted vertically in the inset. a.u., arbitary unit. A full color version of this figure is available at *Polymer Journal* online.

will be discussed later in the Discussion section (Formation of the crystal lattice).

Next, let us explore the changes in the long-range structures detected by the time-resolved SAXS measurements. Figure 2 shows an example of the time evolution of a SAXS profile during the isothermal crystallization at 227 °C. In the figure, the increase in the SAXS intensities accompanied by the appearance of the two peaks indicated by the thick arrows A and B is observed, indicating that lamella structures developed. The details will be discussed in the Discussion section (Development of the long-range structures). Here, we comment on the SAXS profile obtained before the crystal lattice formation at $t = 47$ s (see Figure 1). In the profile, there are no peaks, whereas the intensity in the q-range from 0.08 to 0.15 nm^{-1} is proportional to q^{-4}, corresponding to the so-called Porod's law:[35,36]

$$I(q) \propto (\Delta\rho)^2 S q^{-4} \exp(-\sigma^2 q^2),\ \varepsilon = \sqrt{2\pi}\sigma \tag{2}$$

where $I(q)$ is the scattering intensity, $\Delta\rho$ is the difference in the electron density between two phases, S is the total area of the boundaries between the two phases in the scattering volume, and ε is the interface thickness of the boundaries. Porod's law being exhibited in the SAXS profile obtained at $t = 47$ s, in conjunction with the WAXS profile obtained at $t = 47$ s in Figure 1, indicates that there are neither crystal lattices nor lamella structures but inhomogeneous structure with sharp interfaces with $\varepsilon \sim 0$. The SAXS profile for the melt at $T_i = 264$ °C also exhibits Porod's law, although the slope is slightly steeper than the slope at $t = 47$ s, showing that the inhomogeneous structure in the melt has a slightly thicker interface than the inhomogeneous structure at $t = 47$ s. From Equation 2, we calculated the interface thickness ε from a plot of Iq^4 vs q^2 to obtain $\varepsilon = 17.0$ nm for the melt. It is impossible to evaluate the size of the inhomogeneous structure using the present measurements because of the q-range studied, but it is safe to assume that the inhomogeneous structure is larger than ~75 nm, judging from the low-q limit (0.08 nm^{-1}) in the measurement.

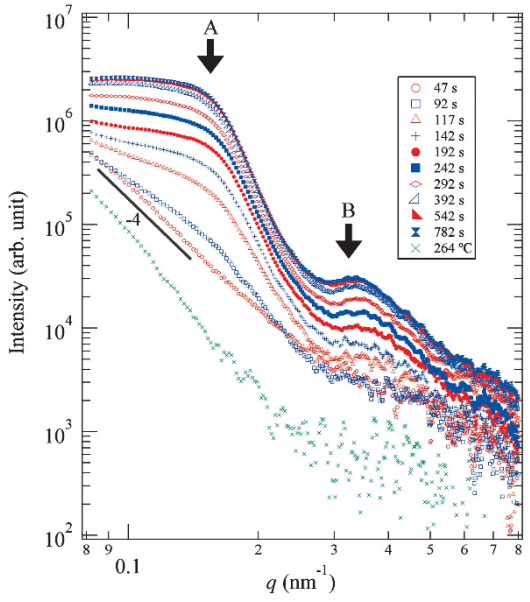

Figure 2 Time evolution of the small-angle X-ray scattering (SAXS) profiles during isothermal crystallization at $T_f = 227$ °C. The scattering profile for the melt at $T_i = 264$ °C (×) is also included. a.u., arbitary unit.

The inhomogeneous structure observed here has so far never been reported, but some small inhomogeneous structures in the amorphous state have been discussed. Wilkes *et al.*[3] found inhomogeneity in the amorphous state and assigned this inhomogeneity to parallel-ordered molecular aggregates of helices with diameters of 2.1–2.2 nm. Pratt *et al.*[4] prepared an ultraquenched amorphous thin film ~100 nm thick for transmission electron microscopy measurements and found a number of nodules 20–25 nm in size on the surface. A nodule is mostly likely an aggregate of the helices observed by Wilkes *et al.*[3] However, the inhomogeneous structure observed in this study is much larger than those reported previously. We have no definite conclusions to make on the inhomogeneous structure, but one possibility is that the inhomogeneous structure is a super-aggregate of the nodules (or molecular aggregates) reported by Wilkes *et al.*[3] and Pratt *et al.*,[4] resulting in fluctuations between dense and less dense regions. We will discuss the inhomogeneous structure using ultra-SAXS data elsewhere.

DISCUSSION

Overall crystallization

To understand the whole crystallization process, we analyzed crystallization rates in terms of the invariant (Q) for SAXS and the degree of crystallinity (ϕ_W) for WAXS, which are defined below. If a material has the spatial variation in the electron density of $\rho(r) = \langle\rho\rangle + \eta(r)$, where $\langle\rho\rangle$ is the average electron density and $\eta(r)$ is the amplitude of the electron density fluctuation from $\langle\rho\rangle$, the mean square of $\eta(r)$, $\langle\eta^2\rangle$, is related to the invariant Q, the total intensity from the system, by[37]

$$\langle\eta^2\rangle \sim Q = 4\pi \int_0^\infty q^2 I(q) \mathrm{d}q. \tag{3}$$

Note that Q reflects all the changes that alter $\langle\eta^2\rangle$. According to Equation 3, the invariant must be calculated for the whole q-range from 0 to infinity, but experimentally $I(q)$ was integrated from $q = 0.08$ nm^{-1} to $q = 1.0$ nm^{-1}. The truncation of the integral range is acceptable in this study because we are interested in the development of the lamella structure that was almost observed in the q-range of our SAXS measurement.

In addition, to evaluate the weight fraction of the crystal, we separated the observed WAXS intensity into the crystal and amorphous contributions, $I_c(q)$ and $I_a(q)$, respectively. In the separation procedure, it was assumed that $I_c(q)$ was a linear combination of Gauss functions and that $I_a(q)$ was a linear combination of Gauss functions and a constant D:

$$I_c(q) = \sum_{i=1}^{i=6} \left[A_i \exp\left\{ -\left(\frac{q - B_i}{C_i} \right)^2 \right\} \right] \tag{4}$$

$$I_a(q) = \sum_{i=7}^{i=8} \left[A_i \exp\left\{ -\left(\frac{q - B_i}{C_i} \right)^2 \right\} \right] + D \tag{5}$$

where $i = 1$ to 6 indicates the diffraction peaks from the crystal and $i = 7$ and 8 indicates the two broad peaks of the amorphous halo. An example of the peak separation is shown in Figure 3 for the data collected at 782 s. We then defined and calculated the degree of crystallinity ϕ_W as follows:

$$\phi_W = \frac{\int_{q1}^{q2} q^2 I_c(q)\, \mathrm{d}q}{\int_{q1}^{q2} q^2 (I_c(q) + I_a(q))\, \mathrm{d}q} \tag{6}$$

where q_1 and q_2 were set to 4 and 20 nm^{-1}, respectively.

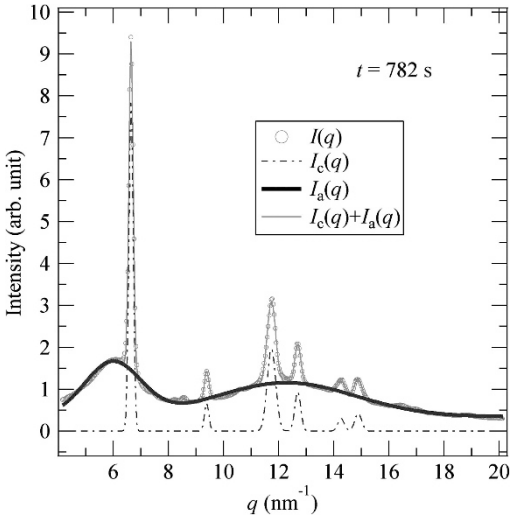

Figure 3 An example of the peak separation using Equations 4 and 5. a.u., arbitary unit. A full color version of this figure is available at *Polymer Journal* online.

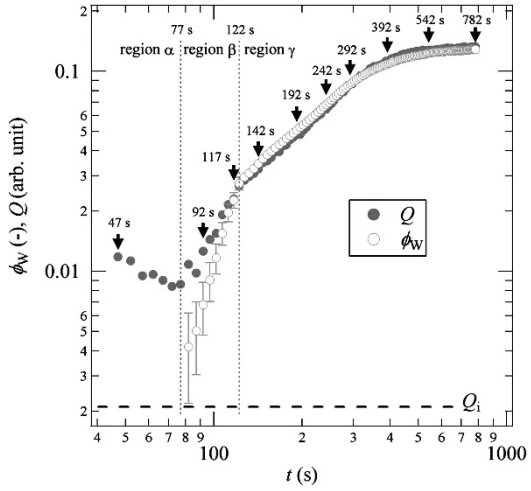

Figure 4 Time evolutions of the degree of crystallinity ϕ_w and the invariant Q, which are evaluated from the time-resolved wide-angle X-ray scattering (WAXS) and small-angle X-ray scattering (SAXS) profiles, respectively, during crystallization at $T_f = 227\,^{\circ}C$. The values of Q were vertically shifted down by multiplying by 2.1×10^{-6} to compare them with ϕ_w. The value of Q for the melt state at $T_i = 264\,^{\circ}C$, Q_i, is indicated by the broken line. The thick arrows show the times t at which the data in Figures 1 and 2 were obtained. a.u., arbitary unit. A full color version of this figure is available at *Polymer Journal* online.

The time evolutions of Q and ϕ_W are shown in Figure 4. Judging from ϕ_W, crystallization started at approximately $t = 77$ s. In the region before $t = 77$ s, which is defined as region α, Q decreases with increasing t, and ϕ_W remains 0. This result indicates that this time region was the induction period before crystallization. The time evolution of the SAXS intensity $I(q)$ in the induction period (region α) is shown in Figure 5 to investigate the origin of the decrease in Q. It is clear that the scattering intensities follow Porod's law ($I(q) \sim q^{-4}$) until $t = 72$ s. According to Equation 2, the decrease in Q in region α reflects a decrease in $\Delta\rho$ or S. If we assume that $\Delta\rho$ is primarily a function of temperature, the decrease in Q indicates a decrease in S.

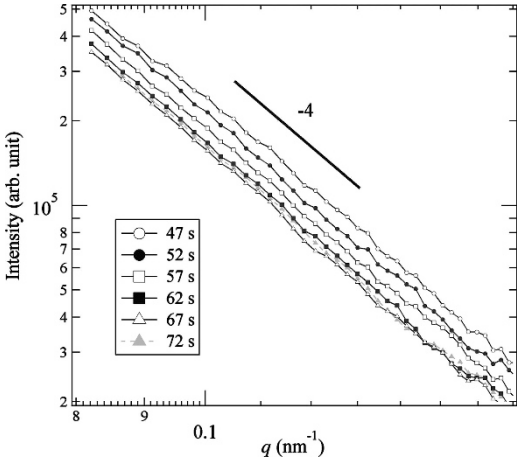

Figure 5 Time-resolved small-angle X-ray scattering (SAXS) profiles between $t = 47$ s and $t = 72$ s. Note that the data are not shifted. a.u., arbitary unit.

Both of the growth rates for Q and ϕ_W changed at $t = 122$ s, after the crystallization started, suggesting that the crystallization mechanism can be divided into two regions. The slope of ϕ_W is larger in the region before $t = 122$ s (region β) than in the region after $t = 122$ s (region γ), showing that the crystallization occurs more rapidly in region β than in region γ. The time evolution of Q shows the same tendency as ϕ_W, indicating that the change in Q, that is, the change in $\langle\eta^2\rangle$, is mainly brought about by the change in ϕ_W, although the slope of Q in region β is smaller than that of ϕ_W. This difference in the slopes between Q and ϕ_W in region β indicates that the inhomogeneous structure still exists and that its scattering also affects Q, at least in region β. The increase in Q brought about by the increase in ϕ_W is partially canceled out by the decrease in Q brought about by the decrease in S (see Figure 5).

The two-step crystallization process in this study was similar to that reported for other polymers, for example, poly(ethylene-*co*-1-octene) (PEOc)[38] and poly(ethylene oxide) (PEOx).[39] In the first process of PEOc and PEOx crystallization, the growth and impingement of spherulites occur, and finally, the sample is filled with spherulites composed of branching and splaying bundles of lamella and amorphous regions between the bundles.[40] The 'bundles' in this study have the same meaning as the 'fibrils' in Figure 3 of Takenaka *et al.*[40] In the bundles, two-phase structures consisting of alternating crystalline lamellae and amorphous regions are built up. In the second process of PEOc and PEOx crystallization, new crystals are nucleated on the bundles and grow in the amorphous regions between the bundles.

Although the case of P4MP1 is similar to the cases of PEOc and PEOx, we found some differences between them through Avrami analysis.[41–43] The result of our Avrami analysis is shown in Figure 6. In the analysis, we used the normalized crystallinity X defined by:

$$X = \frac{\phi_w}{\phi_{w,\infty}} \tag{7}$$

where $\phi_{w,\infty}$ is the value of ϕ_w at the largest t during the experiment. We found that the Avrami constants (n's) are close to 4.0 and to 2.0 in the regions β and γ, respectively. Although Avrami analysis was often applied to many polymer systems to study crystallization kinetics, an Avrami constant of $n = 4$ is not often reported; in the cases of PEOc and PEOx, the n values are < 3 in their first crystallization process

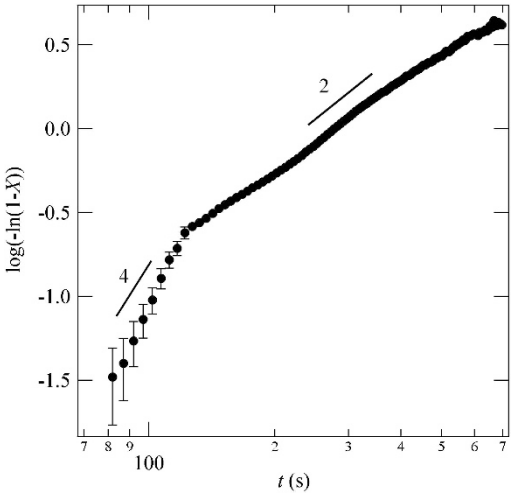

Figure 6 Avrami plot with respect to the normalized crystallinity X defined by Equation 7.

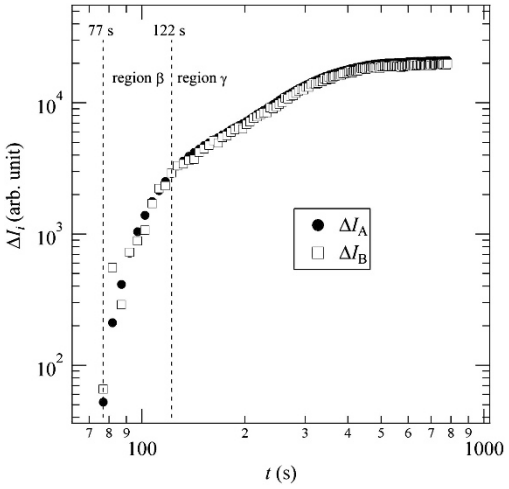

Figure 7 Time evolutions of ΔI_A and ΔI_B, which are the integrated intensities of peaks A and B (see Figure 2), as defined by Equation 9. The values of ΔI_B were vertically shifted up by multiplying by 9.0 to compare with ΔI_A. a.u., arbitary unit.

and approximately 1.0 in their second crystallization process.[38,39] Generally, $n=4$ indicates three-dimensional (3D) crystal growth with homogeneous nucleation, whereas an $n<3$ is understood as n-dimensional growth with heterogeneous nucleation or m-dimensional growth with homogeneous nucleation. Here, $m=n-1$. For the case of $n<3$, the former is more plausible than the latter because heterogeneous nucleation is much faster than homogeneous nucleation. In any case, we have to think about the homogeneous nucleation that occurs in region β for P4MP1. This nucleation could be explained in terms of the inhomogeneous structure consisting of dense and less dense regions. Assuming that nucleation occurs easily in the dense region because the molecular aggregates act as self-nucleation points, we expect a very fast homogeneous nucleation with time in P4MP1.

The difference between the n values in region γ of P4MP1 and in the second crystallization process of PEOc and PEOx reflects the difference in the dimensionality of the crystal growth with heterogeneous nucleation because the bundles act as a nucleation reagent for both P4MP1 and the other two polymers. Hence, $n=2.0$ for P4MP1 and $n=1.0$ for the other two polymers indicate 2D and 1D crystal growths from the bundles, respectively. This difference in the dimensionality of the growth may be related to the difference in the remaining amount of the amorphous region when region γ of P4MP1 starts compared with when the second crystallization process of PEOc and PEOx starts. Region γ of P4MP1 starts at $\phi_w=0.03$, as shown in Figure 4, whereas the second crystallization processes of PEOc and PEOx start at $\phi_w=0.22$–0.24 and $\phi_w=0.30$–0.50, respectively. In the case of P4MP1, once the melt is quenched below the crystallization temperature, the crystallization only proceeds along the relatively dense region of the inhomogeneous structure. Therefore, the less dense regions of the inhomogeneous structure can remain inside and between the spherulites at the end of region β, so P4MP1 could have a larger amorphous region than PEOc and PEOx. This difference in the volume of the amorphous region may allow P4MP1 to crystallize in a higher spatial dimension than the other two polymers.

Development of the long-range structures

In this section, we discuss how the lamella structures develop. As shown in Figure 2, the SAXS profiles, except for the induction period (region α), exhibit the two peaks indicated by the thick arrows A and B. The q-values at the maximum intensities of the peaks A and B are $q_A\sim0.16\,nm^{-1}$ and $q_B\sim0.32\,nm^{-1}$ at $t=782$ s, and the ratio q_A:q_B is 1:2 and does not change during the measurement. This result suggests that peak B is a second order peak of peak A. However, there is the other possibility that two types of lamella structures having different long periods exist in the system. To determine whether peak B is a second order peak of peak A, we evaluated the time evolution of the integrated intensities (I_A and I_B) of peaks of A and B, defined by Equation 8:

$$I_i=\frac{\int_{q_1}^{q_2} q^2 I(q)\mathrm{d}q}{\int_{q_1}^{q_2}\mathrm{d}q} \tag{8}$$

where $i=$ A or B and q_1 and q_2 are $0.08\,nm^{-1}$ and $0.25\,nm^{-1}$ or $0.30\,nm^{-1}$ and $0.60\,nm^{-1}$ for peaks A and B, respectively. We subtracted the amorphous contribution at $t=72$ s from I_A and I_B to evaluate the growth of the intensities because of the crystallization. So we defined Equation 9:

$$\Delta I_i=I_i-I_{i,t=72s} \tag{9}$$

where $I_{i,t=72s}$ is I_i at $t=72$ s. ΔI_A and ΔI_B are plotted as a function of t in Figure 7. In the figure, ΔI_A and ΔI_B overlapped well with each other. We conclude that peak B is the second order peak of peak A, in agreement with the result of the q-ratio as mentioned above, showing that the lamella structures are well ordered.

We then evaluated the time evolution of the lamella thickness (d_c) and the long period (d_{ac}) by calculating the 1D electron density correlation function $k(z)$ developed by Strobl.[44] Here, z indicates the distance in real space. In this calculation, it is assumed that a sample consists of an ensemble of isotropically packed stacks of parallel lamellae and that both the normal and lateral dimensions of these stacks are large compared with the interlamellar distance. In this case, the correlation function $k(z)$ is related to the electron density distribution along the normal of the lamellar surface in a stack. Thus, the $k(z)$ function can be expressed by the scattering intensity

$I(q)$ as follows:

$$k(z) = \frac{\int_0^\infty q^2 I(q) \cos qz \, dq}{\int_0^\infty q^2 I(q) \, dq} \quad (10)$$

experimentally integrated from $q = 0.08\,nm^{-1}$ to $q = 0.30\,nm^{-1}$. As there is not enough intensity in the q-region above $0.30\,nm^{-1}$ to calculate $k(z)$ without error, we set the upper limit of the integration at $0.30\,nm^{-1}$. Hence, the information from peak B is missing, but this is not that important because peak B is the second order peak of peak A, as already discussed. Therefore, our experimental integral range is acceptable for the same reason mentioned for Q. An example of the calculated $k(z)$ is shown for $t = 782\,s$ in Figure 8, and we can evaluate d_c and d_{ac}. The obtained d_c and d_{ac} are plotted as functions of the time t in Figure 9. As shown in the figure, d_{ac} decreases with increasing t, mainly in region β, indicating that new lamellae were formed not only in the amorphous region between the bundles but also in the amorphous region between the existing lamellae in the bundles. On the other hand, d_c is constant throughout the whole crystallization process. This result is quite different from the polyethylene result. In the case of polyethylene,[45,46] a continuous increase in d_c occurs, and the thickening of the lamella is explained by the existence of the α_c–process, which corresponds to longitudinal chain diffusion inside the crystals.[47] In the case of syndiotactic polypropylene,[48] on the other hand, lamella thickening does not occur, which is explained by the α_c–process not occurring in syndiotactic polypropylene.[49] Our result on P4MP1 is the same as that for syndiotactic polypropylene. These results may indicate that, in the case of P4MP1, the longitudinal chain diffusion inside the crystals is depressed by the *interlocking* of the side groups and thus did not occur in our experiment. Note that the α_c–process and the thickening of the lamella for P4MP1 were observed under non-isothermal conditions; relaxation just below the melting point was observed by measurements of the dynamic viscoelasticity from –150 to 200 °C[50] and an increase in lamella thickness was observed when samples prepared at a temperature T_1 were annealed at another temperature T_2.[23,26] Here, $T_1 < T_2$. In these cases, no one can completely deny the possibility of a melt and re-crystallization, which is the other possible process in addition to thickening. However, for the purpose of discussion, we assume that the α_c–process and thickening occurred in these cases. According to the so-called Gibbs–Thomson equation,[51] d_c becomes larger as T_m becomes larger. Therefore, $T_1 < T_2$ indicates that there is a thermodynamic driving force behind thickening, which may be necessary for the longitudinal chain diffusion of P4MP1. In our experiment, the temperature was changed from T_i to T_f directly and the crystallization process was observed at T_f; therefore, our experiment corresponds to the case of $T_1 = T_2$, where there is no thermodynamic driving force for thickening.

Formation of the crystal lattice

We now explore the changes in the size of the tetragonal unit cell, which was briefly pointed out in the Results section. The lattice constant a calculated from the (200) diffraction peak and the half-width at half-maximum (σ) of the peak are plotted as functions of t in Figure 10. Here, we note that we could not evaluate the lattice constant c of the c-axis in this study because the (007) diffraction peak, which is most strong among the diffraction peaks from the lattice planes that are perpendicular to c-axis,[5] was out of the q-range of our measurement, and the diffraction peaks that were in the q-range of our measurement and have information about c-axis

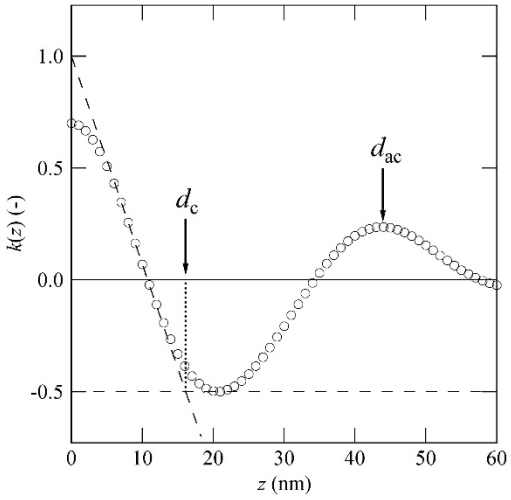

Figure 8 An example of a one-dimensional electron density correlation function $k(z)$ defined by Equation 10. d_c and d_{ac} are obtained as z-values at the heads of the arrows indexed by d_c and d_{ac}, respectively.

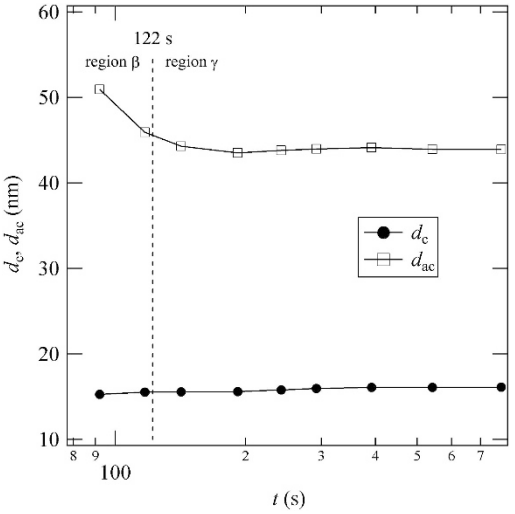

Figure 9 Time evolutions of the thickness of the lamella d_c and the long period d_{ac} during crystallization at $T_f = 227$ °C.

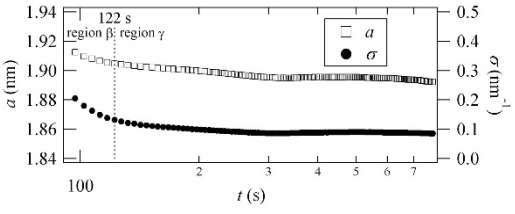

Figure 10 Time evolutions of the lattice constant a and the half-width at half-maximum σ of the (200) diffraction peak during crystallization at $T_f = 227$ °C.

were too weak or overlap too much with other peaks to enable the evaluation of the lattice constant *c*. As shown in Figure 10, *a* and σ decreased with increasing *t*, indicating that the initial formation of the crystal lattice occurred under kinetic control, and then the crystal lattice changed to the more stable state. The changes were more rapid in region β than in region γ. The same type of change reported for P4MP1 was reported for PEOc.[38] In the case of PEOc, the side groups in the 1-octene unit (0.21 mol%) behaved as defects, and the stabilization of the crystals via removal of the defects results in decreases in the lattice constants *a* and *b* and in the width of the diffraction peaks. In the case of P4MP1, on the other hand, the side groups of the helical chains were not defects. Kusanagi *et al.*[5] studied the crystal structure of P4MP1 using WAXS data, as well as an energy calculation, and determined that the side groups are *interlocked* with each other in the plane perpendicular to the *c*-axis. Refining the structure by calculating the energy of the crystal lattice, taking into account the intra- and intermolecular interactions, they found that in the most stable crystal structure, the rotational angles of the C–C bond in the side group were distorted and distributed over a wide range because of side group *interlocking*. The distortion increases the side group energy but reduces the distance between the backbone chains, resulting in a reduction in the total crystal energy. We expect that the rotational angles of the C–C bond in the side groups were not distorted just after crystal formation from the melt. But during the stabilization process (region β in Figure 10), the rotational angles were distorted, leading to a reduction in the lattice constant of the *a*-axis. Note that a reduction in the lattice constant *c* of the *c*-axis could not have occurred during the stabilization process because the lamella thickness d_c did not change (see Figure 9), which suggests that the interlocking and distortion of the side groups are not related to the *c*-axis.

CONCLUSION

We studied the crystallization process of P4MP1 under an isothermal condition at 227 °C using time-resolved simultaneous SAXS and WAXS measurements and found that the crystallization process consisted of a first process (region β) and a second process (region γ). From the Avrami analysis, we expected 3D crystal growth with homogeneous nucleation in region β and 2D growth with heterogeneous nucleation from the bundles in region γ. The homogeneous nucleation in region β is explained by the inhomogeneous structure observed in the SAXS data in the melt, and the 2D growth in region γ, which was larger than the growth dimensionality in the second crystallization process of other polymers (PEOc and PEOx), was assigned to the large amount of remaining amorphous region when region γ started.

During the crystallization, especially in region β, it was found that the lattice constant *a* and the half-width at half-maximum (σ) of the peak decreased with the annealing time, whereas the thickness of the lamella d_c remained constant. These features are explained by the *interlocking* between the side groups. The rotational angles in the interlocked side groups are distorted during crystallization, reducing the lattice constant *a*, whereas the interlocking inhibits the longitudinal chain diffusion along the chain axis, keeping the lamella thickness unchanged.

ACKNOWLEDGEMENTS

The SAXS and WAXS measurements in this work were conducted with the approval of SPring-8 (Grant Nos. 2010A7229, 2010B7274, 2011A7220 and 2011B7270).

1 Zoller, P., Starkweather, J. H. W. & Jones, G. A. The heat of fusion of Poly(4-methylpentene-1). *J. Polym. Sci. B. Polym. Phys.* **24,** 1451–1458 (1986).
2 Charlet, G. & Delmas, G. Heat of fusion of Poly(4-methylpentene-1). *J. Polym. Sci. B. Polym. Phys.* **26,** 1111–1125 (1988).
3 Wilkes, C. E. & Lehr, M. H. J. Evidence for ordered molecular aggregates in the amorphous and molten states of poly(4-methylpentene-1). *Macromol. Sci. Phys.* **B7,** 225–230 (1973).
4 Pratt, C. F. & Geil, P. H. Chain mobility and crystallization in ultraquenched glasses of polypivalolactone and poly(4-methyl-pentene-1). *J. Macromol. Sci.* **B21,** 617–649 (1982).
5 Kusanagi, H., Takase, M., Chatani, Y. & Tadokoro, H. Crystal structure of isotactic poly(4-methyl-1-pentene). *J. Polym. Sci., Polym. Phys. Ed.* **16,** 131–142 (1978).
6 Natta, G., Corradini, P. & Bassi, I. W. The crystalline structure of several isotactic polymers of α-olefins. *Rend. Fis. Acc. Lincei.* **19,** 404–411 (1955).
7 Frank, F. C., Keller, A. & O'Connor, A. Observations on single crystals of an isotactic polyolefin: Morphology and chain packing in poly-4-methyl-pentene-1. *Philos. Mag.* **8,** 200–214 (1959).
8 Bassi, I. W., Bonsignori, O., Lorenzi, G. P., Pino, P., Corradini, P. & Temussi, P. A. Structure and optical activity of a crystalline modification of isotactic poly-(S)-4-methyl-1-hexene. *J. Polym. Sci., Polym. Phys. Ed.* **9,** 193–208 (1971).
9 Tanda, Y., Kawasaki, N., Imada, K. & Takayanagi, M. New crystal modifications of isotactic poly-4-methyl-pentene-1. *Rep. Prog. Polym. Phys. Jpn.* **9,** 165 (Reserch Group of Polymer Physics in Japan, Tokyo, 1966).
10 Kawasaki, N. & Takayanagi, M. Conformational effect of normal and branched side chains of poly-α-olefins on crystalline viscoelastic dispersions. *Rep. Prog. Polym. Phys. Jpn.* **10**, 337 (Reserch Group of Polymer Physics in Japan, Tokyo, 1967).
11 Takayanagi, M. & Kawasaki, N. Mechanical relaxation of poly-4-methyl-pentene-1 at cryogenic temperatures. *J. Macromol. Sci.-Phys.* **B1,** 741–758 (1967).
12 Charlet, G. & Delmas, G. Effect of solvent on the polymorphism of poly(4-methylpentene-1). 2. Crystallization in semi-dilute solutions. *Polymer* **25,** 1619–1625 (1984).
13 Nakajima, A., Hayashi, S., Taka, T. & Utsumi, N. Effect of solvent on morphology of poly(4-methyl-1-pentene) single crystals crystallized from various solvents. *Kolloid. Z. Z. Polym.* **234,** 1097–1108 (1969).
14 Nakajima, A., Hayashi, S. & Taka, T. Melting behavior of poly(4-methyl-1-pentene) single crystals. *Kolloid. Z. Z. Polym.* **233,** 869–878 (1969).
15 Charlet, G., Delmas, G., Revol, F. J. & Manley, St J R. Effect of solvent on the polymorphism of poly(4-methyl-1-pentene). 1. Solution-grown single crystals. *Polymer* **25,** 1613–1618 (1984).
16 De Rosa, C., Borriello, A., Venditto, V. & Corradini, P. Crystal structure of form III and the polymorphism of isotactic poly(4-methylpentene-1). *Macromolecules* **27,** 3864–3868 (1994).
17 De Rosa, C., Auriemma, F., Borriello, A. & Corradini, P. Up-down disorder in the crystal structure of form III of isotactic poly(4-methyl-1-pentene). *Polymer* **36,** 4723–4727 (1995).
18 De Rosa, C., Capitani, D. & Cosco, S. Solid-state 13C nuclear magnetic resonance spectra of four crystalline forms of isotactic poly(4-methyl-1-pentene). *Macromolecules* **30,** 8322–8331 (1997).
19 Hasegawa, R., Tanabe, Y., Kobayashi, M., Tadokoro, M., Sawaoka, A. & Kawai, N. Structural studies of pressure-crystallized polymers. I. Heat treatment of oriented polymers under high pressure. *J. Polym. Sci., Polym. Phys. Ed.* **8,** 1073–1087 (1970).
20 Charlet, G. & Delmas, G. 'Modification V' of poly(4-methyl-1-pentene) from cyclopentane solutions and gels. *Polym. Bull.* **6,** 367–373 (1982).
21 De Rosa, C. Chain conformation of form IV of isotactic poly(4-methyl-1-pentene). *Macromolecules* **32,** 935–938 (1999).
22 Tanigami, T. & Miyasaka, K. Small-angle X-ray scattering of isotactic poly(4-methyl-1-pentene). *J. Polym. Sci. Polym. Phys. Ed.* **19,** 1865–1871 (1981).
23 Silvestre, C., Cimmino, S., Di Pace, E., Di Lorenzo, M. L., Orsello, G., Karasz, F. E. & Lin, J. S. Morphology development of isotactic poly(4-methylpentene-1) during melt crystallization. *J. Mater. Sci.* **36,** 2865–2874 (2001).
24 Griffith, J. H. & Rånby, B. G. Dilatometric measurements on poly(4-methyl-1-pentene) glass and melt transition temperatures, crystallization rates, and unusual density behavior. *J. Polym. Sci.* **44,** 369–381 (1960).
25 Patel, D. & Bassett, D. C. On spherulitic crystallization and the morphology of melt-crystallized poly(4-methylpentene-1). *Proc. R Soc. Lond. A Math. Phys. Sci.* **445,** 577–595 (1994).
26 Bassett, D. C. & Patel, D. Isothermal lamellar thickening and the distribution of thermal stability in spherulitic isotactic poly(4-methylpentene-1). *Polymer* **35,** 1855–1862 (1994).
27 Chen, S., Jin, J. & Zhang, J. Non-isothermal crystallization behaviors of poly(4-methyl-pentene-1). *J Therm. Anal. Calorim.* **103,** 229–236 (2011).
28 Yadav, Y. S., Jain, P. C. & Nanda, V. S. Use of differential scanning calorimetry to study polymer crystallization kinetics with longer half times. *Thermochim. Acta* **71,** 313–321 (1983).
29 Charlet, G. & Delmas, G. Heat of fusion of poly(4-methylpentene-1). *J. Polym. Sci. B Polym. Phys.* **26,** 1111–1125 (1988).
30 Rastogi, S., Newman, M. & Keller, A. Pressure-induced amorphization and disordering on cooling in a crystalline polymer. *Nature* **353,** 55–57 (1991).
31 Hoffman, J. D. & Weeks, J. J. Rate of spherulitic crystallization with chain folds in polychlorotrifluoroethylene. *J. Chem. Phys.* **37,** 1723–1741 (1962).

32 Silvestre, C., Cimmino, S., Di Pace, E. & Monaco, M. Morphology and crystallization of poly(4-methylpentene-1) and its blends with hydrogenated oligocyclopentadiene. *J. Macromol. Sci. Pt A* **35,** 1507–1525 (1998).
33 Masunaga, H., Ogawa, H., Takano, T., Sasaki, S., Goto, S., Tanaka, T., Seike, T., Takahashi, S., Takeshita, K., Nariyama, N., Ohashi, H., Ohata, T., Furukawa, Y., Matsushita, T., Ishizawa, Y., Yagi, N., Takata, M., Kitamura, H., Sakurai, K., Tashiro, K., Takahara, A., Amamiya, Y., Horie, K., Takenaka, M., Kanaya, T., Jinnai, H., Okuda, H., Akiba, I., Takahashi, I., Yamamoto, K., Hikosaka, M., Sakurai, S., Shinohara, Y., Okada, A. & Sugihara, Y. Multipurpose soft-material SAXS/WAXS/GISAXS beamline at SPring-8. *Polym. J.* **43,** 471–477 (2011).
34 Fujimura, M., Hashimoto, H., Kurahashi, K., Hashimoto, T. & Kawai, H. Domain-boundary structure of styrene-isoprene block copolymer films cast from solutions. 6. Effect of temperature on spherical microdomain structure. *Macromolecules* **14,** 1196–1202 (1981).
35 Porod, G. Die Röntgenkleinwinkelstreuung von dichtgepackten kolloiden Systemen I. Teil. *Kolloid Z* **124,** 83–114 (1951).
36 Porod, G. Die Röntgenkleinwinkelstreuung von dichtgepackten kolloiden Systemen II. Teil. *Kolloid Z* **125,** 51–57 (1952).
37 Roe, R. J. *Methods of X-ray and Neutron Scattering in Polymer Science* (Oxford, New York, 2000).
38 Akpalu, Y., Kielhorn, L., Hsiao, B. S., Stein, R. S., Russell, T. P., van Egmond, J. & Muthukumar, M. Structure development during crystallization of homogeneous copolymers of ethene and 1-octene: time-resolved synchrotron X-ray and SALS measurements. *Macromolecules* **32,** 765–770 (1999).
39 Lisowski, M. S., Liu, Q., Cho, J., Runt, J., Yeh, F. & Hsiao, B. S. Crystallization behavior of poly(ethylene oxide) and its blends using time-resolved wide- and small-angle X-ray scattering. *Macromolecules* **33,** 4842–4849 (2000).
40 Takenaka, M., Shimizu, H. & Nishitsuji, S. Butterfly patterns in crystalline polymers under uniaxial stretch. *Phys. Rev. E* **75,** 061802 (2007).
41 Avrami, M. Kinetics of phase change. I general theory. *J. Chem. Phys.* **7,** 1103–1112 (1939).
42 Avrami, M. Kinetics of phase change. II transformation-time relations for random distribution of nuclei. *J. Chem. Phys.* **8,** 212–224 (1940).
43 Avrami, M. Granulation, phase change, and microstructure kinetics of phase change. III. *J. Chem. Phys.* **9,** 177–184 (1941).
44 Strobl, G. *The Physics of Polymers* (Springer, Berlin, 2007).
45 Albrecht, T. & Strobl, G. Temperature-dependent crystalline-amorphous structures in linear polyethylene: surface melting and the thickness of the amorphous layers. *Macromolecules* **28,** 5827–5833 (1995).
46 Albrecht, T. & Strobl, G. Observation of the early stages of crystallization in polyethylene by time-dependent SAXS: transition from individual crystals to stacks of lamellae. *Macromolecules* **29,** 783–785 (1996).
47 Men, Y., Rieger, J., Endeler, H. & Lilge, D. Mechanical α-process in polyethylene. *Macromolecules* **36,** 4689–4691 (2003).
48 Schmidtke, J., Strobl, G. & Thurn-Albrecht, T. A four-state scheme for treating polymer crystallization and melting suggested by calorimetric and small angle X-ray scattering experiments on syndiotactic polypropylene. *Macromolecules* **30,** 5804–5821 (1997).
49 Sakata, Y., Unwin, A. P. & Ward, I. M. The structure and mechanical properties of syndiotactic polypropylene. *J. Mater. Sci.* **30,** 5841–5849 (1995).
50 Tanigami, T., Yamaura, K., Matsuzawa, S. & Miyasaka, K. Thermal expansion of crystal lattice of isotactic poly(4-methyl-1-pentene). *Polym. J.* **18,** 35–40 (1986).
51 Wunderlich, B. *Macromolecular Physics 3 Crystal Melting* (Academic Press, New York, 1980).